Predicting absorption characteristics of single-leaf permeable membrane absorbers using finite element method in a time domain

Okuzono, Takeshi
Shimizu, Noriyasu
Sakagami, Kimihiro

(Citation)
Applied Acoustics,151:172-182

(Issue Date)
2019-08

(Resource Type)
journal article

(Version)
Accepted Manuscript

(URL)
https://hdl.handle.net/20.500.14094/90005905

Predicting absorption characteristics of single-leaf permeable membrane absorbers using finite element method in a time domain

Takeshi Okuzono[a,1] Noriyasu Shimizu[a] and Kimihiro Sakagami[a]

[a] *Environmental Acoustic Laboratory, Department of Architecture, Graduate School of Engineering, Kobe University, 1-1, Rokkodai, Nada, Kobe 657-8501, Japan*

Abstract

Permeable membranes (PMs), which are air-permeable thin woven fabrics or non-woven fabrics, are attractive sound-absorbing materials used to control acoustics in buildings. Although the absorption characteristics of various PM absorbers have been studied extensively, it has not been established how to incorporate PMs into a wave-based acoustic simulation method known as the time-domain finite element method (TD-FEM). This paper presents a numerical model of limp PMs for TD-FEM as well as a computationally efficient TD-FEM for predicting sound fields including PMs. The limp PM model incorporates effects of both sound-induced vibration of PMs and the air permeability of PMs. Consequently, two material parameters are considered: the surface density and flow resistance of PMs. Verification of the limp PM model and efficiency evaluation of TD-FEM were first performed with an impedance tube problem. Then, reverberation absorption coefficients of single-leaf PM absorbers with a non-locally reacting rigid backed air cavity were predicted through simulation of a reverberation absorption coefficient measurement using the present TD-FEM at frequencies of 100 Hz to 2.5 kHz. The predicted results were compared with measured and theoretical values. To demonstrate the applicability of present TD-FEM, eight PMs, each with different flow resistance and surface density, were considered for comparison. Results revealed that the present TD-FEM with the limp PM model

[1] Corresponding author. Tel./fax: +81 78 803 6577.
E-mail address: okuzono@port.kobe-u.ac.jp (T. Okuzono).

can predict the magnitude relation of absorption characteristics of single-leaf PM absorbers attributable to differences of material properties of PMs.

Keywords: Fabric, Non-woven fabric, Room acoustics, Sound absorption, Textile, Time domain finite element method

1. Introduction

Sound absorbers play an important role in creating comfortable acoustic environments in buildings by controlling reverberation times and reducing noise levels. For this purpose, permeable membrane (PM) absorbers have been recognized as attractive sound absorbing structures. PM absorbers are a sound absorbing structure using PMs, which are an air-permeable thin woven fabric or non-woven fabric made from natural or chemical fibers. Actually, PMs can be made lightweight and translucent. A wide range of functional designs is possible for PMs through combinations of fibers and manufacturing and processing methods. Furthermore, non-woven fabrics are cost-efficient materials because of their high productivity. With those attractive features, acoustic properties of PMs have been studied extensively. In fact, various PM absorbers have been proposed to date, such as acoustic curtains, suspended acoustic ceilings, and space sound absorbers. Such PM absorbers have been applied successfully to various architectural spaces such as conference rooms, stadiums, swimming pools, and churches.

The simplest PM absorber is a single-leaf PM absorber in which a PM is placed in front of a rigid-backed air cavity. An example of the absorber is an air-permeable curtain placed in front of a wall or a window. The absorption characteristics of single-leaf PM absorbers using rigid and limp PMs have been studied theoretically in cases with and without honeycomb cores inside a backing air cavity [1]. Takahashi *et al.* [2] have presented a predictive model of sound absorption and transmission through a single-leaf PM. The model is based on a Helmholtz integral for sound field coupled with the equation of motion of a membrane. They also presented a predictive method for a multilayered structure with PM facings. Sakagami *et al.* [3] theoretically analyzed acoustical properties of a single-leaf PM using an equivalent circuit analogy. That report described details of the effects of material properties of PM on the resulting acoustical performance. Pieren [4] used a limp model to study absorption characteristics of thin woven fabrics backed by an air cavity and presented a geometry-based model for obtaining the air flow re-

sistance of thin woven fabric. Absorption characteristics of double-leaf PM structures and three-dimensional PM space absorbers have been investigated in some studies reported in the literature [5, 6]. The three-dimensional PM space absorbers can be placed freely inside rooms, with combined usage of lighting equipment. A predictive model of the absorption characteristics of multilayered curtains can be found in the literature [7].

The applicability and practicality of time domain wave-based numerical methods intended for usage in room acoustics design have advanced considerably in recent years along with frequency domain methods. To date, various time domain wave-based methods have been proposed with unique strengths and shortcomings. They have also been applied to room acoustics simulation. For example, the finite difference time domain (FDTD) method is an efficient solver [8, 9, 10] with strengths of simplicity in formulation and implementation. In addition, the algorithm is generally explicit. However, as a shortcoming, staircase approximation is introduced at boundary surfaces because of discretization on a rectangular grid. Time-domain - finite element method (TD-FEM) [11, 12, 13, 14] is inherently useful for the modeling of complex geometries with finite element discretization of space. In addition, unconditional stability is obtained in the standard formulation. Derivation of the stability condition is simple, even in sound field analyses of complexly shaped rooms using a conditionally stable algorithm. However, the algorithm is generally implicit. The implementation is more difficult than that using the FDTD method. Other attractive time domain methods are found in reports of the literature [15, 16, 17]. Among the various time domain methods, this report specifically addresses sound absorber modeling using TD-FEM for acoustics simulation.

An earlier work on TD-FEM presented an equivalent impedance model [12, 13] used as a simple model to address the absorption characteristics of various sound absorbers. The model, which is based on the assumption of local reaction, uses constant real-valued surface impedance in the frequency ranges of interest. However, it cannot consider the frequency and incident angle dependence of absorption characteristics of sound absorbers accurately. Therefore, the development of proper sound absorber models is important to increase the applicability and accuracy of TD-FEM on room acoustics simulation. It is also true for PM absorbers described above. For example because absorption characteristics of single-leaf PM absorbers with a rigid backed air cavity depend strongly on both the frequency and incident sound angle [1], it can be expected that the equivalent impedance model cannot accurately capture

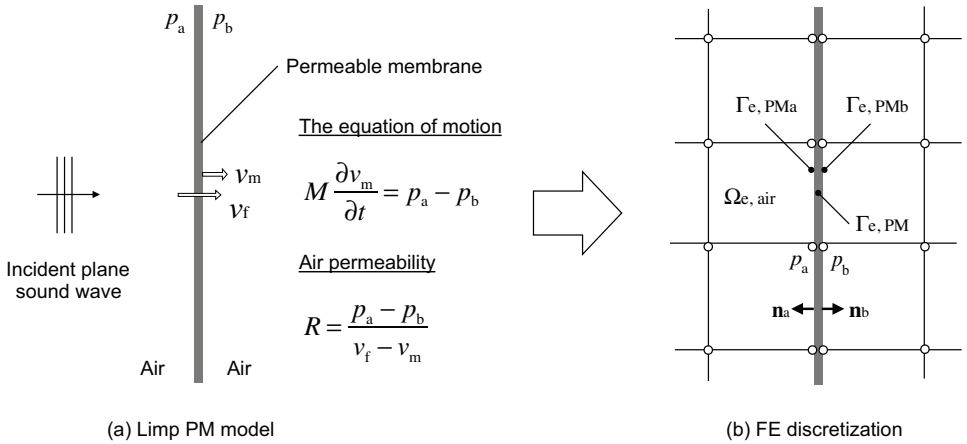

Figure 1: Limp permeable membrane model and a spatially discretized FE model.

the absorption characteristics of acoustic curtains and suspended acoustic ceilings using PMs.

This study was conducted (1) to develop a numerical model of limp PMs for TD-FEM as well as a computationally efficient TD-FEM for predicting sound fields including PMs and (2) to demonstrate their applicability. The present method would be useful to analyze sound fields in rooms including various PM absorbers such as acoustic curtains, suspended ceiling absorbers, and space absorbers. The remainder of the present paper is organized as follows. Section 2 presents a description of a theory of limp PM finite elements (FEs). Eight-node hexahedral limp PM FEs are derived for three-dimensional analyses. The limp PM FEs are incorporated further into an efficient TD-FEM, which has been presented in our previous paper [13]. In Sec. 3, limp PM FEs are verified using an impedance tube problem. The convergence property of present TD-FEM with the limp PM elements is tested. Section 4 demonstrates the applicability of TD-FEM with the limp PM FEs, where reverberation absorption coefficients of eight single-leaf PM absorbers are predicted by simulation of reverberation absorption coefficient measurements. We compared our results with those measured in an irregularly shaped reverberation room and with a theoretically calculated statistical absorption coefficient. The present paper is concluded in Sec. 5. The present paper is an extension of our brief paper [18] which deals with two-dimensional analyses. Hereinafter, we will present more detailed discussion on the accuracy of the present method in three-dimensional analyses.

2. Theory

2.1. Boundary condition of limp permeable membrane

The present PM model is based on the limp membrane FEs in the frequency domain [19]. This section presents derivation of the time domain boundary conditions of PMs. In this paper, a PM is assumed to be limp considering that the interaction between the sound incident wave and the membrane results in the sound-induced motion of the membrane. The equation of motion for limp PM is given as

$$M\frac{\partial v_{\mathrm{m}}}{\partial t} = p_{\mathrm{a}} - p_{\mathrm{b}}, \tag{1}$$

where M, v_{m}, and t respectively denote the surface density of PM, the vibration velocity of PM and time. The right-hand-side of Eq. (1) $p_{\mathrm{a}} - p_{\mathrm{b}}$ represents the sound pressure difference between both sides of PM. The effect of air permeability of material is modeled by the definition of flow resistance R, which is assumed as a purely resistive value and which is defined as

$$R = \frac{p_{\mathrm{a}} - p_{\mathrm{b}}}{v_{\mathrm{f}} - v_{\mathrm{m}}}, \tag{2}$$

where v_{f} represent the particle velocity on and inside PM. Figures 1(a) and 1(b) respectively show the limp PM model and a spatially discretized FE model of limp PM, where $\Omega_{\mathrm{e,air}}$ is the air finite element, and $\Gamma_{\mathrm{e,PM}}$ is the limp membrane finite element with two boundary surfaces $\Gamma_{\mathrm{e,PMa}}$ and $\Gamma_{\mathrm{e,PMb}}$. In addition, $\mathbf{n}_{\mathrm{a}}$ and $\mathbf{n}_{\mathrm{b}}$ represent the normal vectors at boundary surfaces of PM. In the present time domain formulation, the limp PM model is incorporated for vibration boundary conditions on both boundary surfaces of PM. The vibration boundary conditions are

$$\frac{\partial p}{\partial n} = \begin{cases} -\rho_0 \dot{v}_{\mathrm{f}} & \text{on } \Gamma_{\mathrm{e,PMa}}, \\ \rho_0 \dot{v}_{\mathrm{f}} & \text{on } \Gamma_{\mathrm{e,PMb}}. \end{cases} \tag{3}$$

In those equations, ρ_0 denotes the air density and $\cdot$ signify the first-order derivative with respect to time. The first-order derivative value of particle velocity is calculated from Eqs. (1) and (2) as

$$\dot{v}_{\mathrm{f}} = \frac{1}{R}(\dot{p}_{\mathrm{a}} - \dot{p}_{\mathrm{b}}) + \frac{1}{M}(p_{\mathrm{a}} - p_{\mathrm{b}}), \tag{4}$$

where time factor $\exp(i\omega t)$ is assumed with the imaginary unit i and the angular frequency ω.

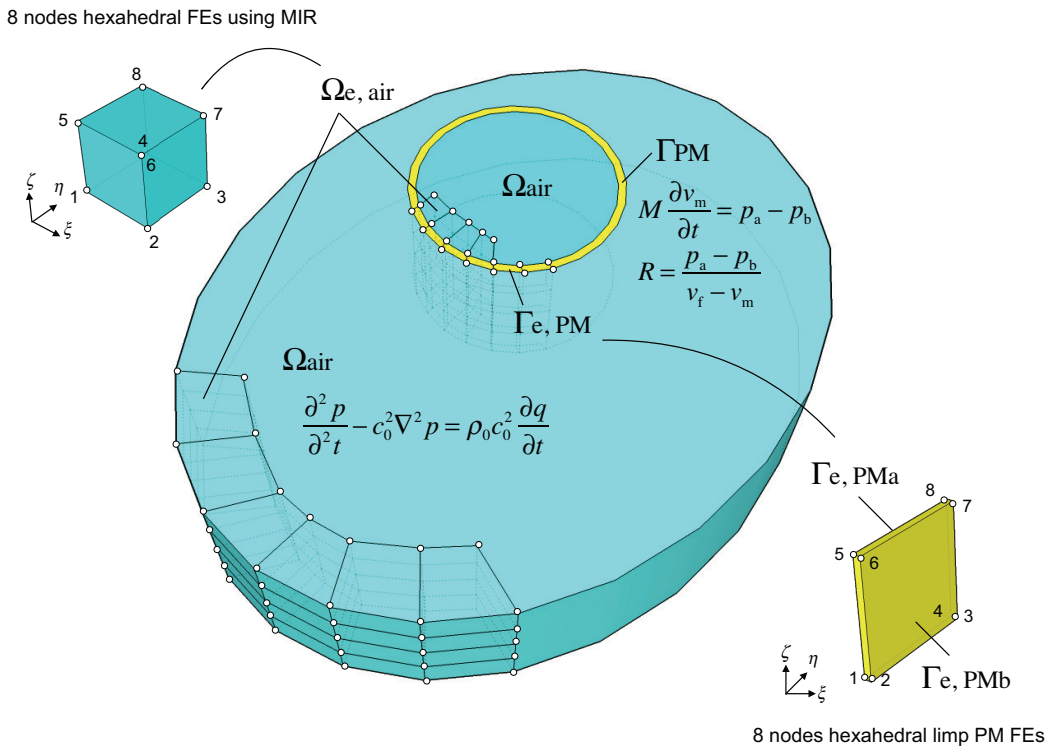

Figure 2: Spatially discretized sound field including permeable membranes. The air domain Ω_{air} is discretized by the air FEs $\Omega_{\text{e,air}}$ called eight-node hexahedral FEs using MIR, and the permeable membrane Γ_{PM} is discretized using eight node-hexahedral limp PM FEs.

2.2. Spatial and time discretization of a sound field including PM

We consider sound propagation in a closed sound field including PM. The present formulation of TD-FEM is based on our earlier work [13], which does not address the modeling of PMs. Also, TD-FEM is fourth-order accurate with respect to dispersion error for an idealized case, i.e., the sound propagation in a free field discretized by rectangular FEs. Furthermore, TD-FEM has two appealing characteristics: relaxation of stability condition and faster convergence of an iterative solver. Hereinafter, the complete formulation of TD-FEM is presented including how to incorporate the limp PM model described above.

As presented in Fig. 2, sound propagation in the air domain Ω_{air} is described by the nonhomogeneous wave equation expressed in sound pressure

p

$$\frac{\partial^2 p}{\partial^2 t} - c_0^2 \nabla^2 p = \rho_0 c_0^2 \frac{\partial q}{\partial t}, \tag{5}$$

where c_0 is the speed of sound in air and q is the added fluid mass per unit volume. The air domain Ω_{air} is discretized by eight-node hexahedral FEs with a dispersion reduction method known as modified integration rules (MIR) [20]. Details of FEs are described in reports of the literature [13]. The weak form of nonhomogeneous wave equation is given as

$$\int_{\Omega_{\mathrm{air}}} \phi \frac{\partial^2 p}{\partial^2 t} dV + c_0^2 \int_{\Omega_{\mathrm{air}}} \nabla \phi \nabla p dV = c_0^2 \int_{\Gamma} \phi \frac{\partial p}{\partial n} dA + \rho_0 c_0^2 \int_{\Omega_{\mathrm{air}}} \phi \frac{\partial q}{\partial t} dV, \tag{6}$$

where ϕ, dA, and dV respectively represent the arbitrary weight function, surface integral, and volume integral. The symbol Γ represents the domain boundary. Here, the four boundary conditions are the rigid boundary Γ_0, vibration boundary Γ_{v}, impedance boundary Γ_{Z}, and PM boundary Γ_{PM}. Introducing finite element approximations to the sound pressure and the weight function gives the following semi-discretized equation as

$$\begin{aligned} &\textstyle\sum_{\mathrm{e}}^{n_{\mathrm{e}}} \Big[\int_{\Omega_{\mathrm{e,air}}} \boldsymbol{N}^{\mathrm{T}} \boldsymbol{N} dV \ddot{\boldsymbol{p}}_{\mathrm{e}} + c_0^2 \int_{\Omega_{\mathrm{e,air}}} \nabla \boldsymbol{N}^{\mathrm{T}} \nabla \boldsymbol{N} dV \boldsymbol{p}_{\mathrm{e}} \\ &- c_0^2 \int_{\Gamma_{\mathrm{e,v}}+\Gamma_{\mathrm{e,Z}}+\Gamma_{\mathrm{e,PM}}} \boldsymbol{N}^{\mathrm{T}} \frac{\partial p}{\partial n} dA \Big] = \textstyle\sum_{\mathrm{e}}^{n_{\mathrm{e}}} \Big[\rho_0 \int_{\Omega_{\mathrm{e,air}}} \boldsymbol{N}^{\mathrm{T}} \dot{q} dV \Big], \end{aligned} \tag{7}$$

where $\boldsymbol{p}_{\mathrm{e}}$, $\boldsymbol{N}$, and n_{e} represent the nodal sound pressure vector, the shape function and total numbers of elements. Symbols $\ddot{\cdot}$, $\Gamma_{\mathrm{e,v}}$, and $\Gamma_{\mathrm{e,Z}}$ respectively signify the second-order derivative with respect to time, vibration boundary element, and impedance boundary element. Regarding the PM boundary, with the boundary condition of Eq. (3) the boundary condition term in Eq. (7) can be written as

$$\int_{\Gamma_{\mathrm{e,PM}}} \boldsymbol{N}^{\mathrm{T}} \frac{\partial p}{\partial n} dA = \int_{\Gamma_{\mathrm{e,PMa}}} \boldsymbol{N}^{\mathrm{T}} \frac{\partial p}{\partial n} dA + \int_{\Gamma_{\mathrm{e,PMb}}} \boldsymbol{N}^{\mathrm{T}} \frac{\partial p}{\partial n} dA = \frac{\rho_0}{R} \boldsymbol{S}_{\mathrm{e}} \dot{\boldsymbol{p}}_{\mathrm{e}} + \frac{\rho_0}{M} \boldsymbol{S}_{\mathrm{e}} \boldsymbol{p}_{\mathrm{e}}, \tag{8}$$

where the element matrix $\boldsymbol{S}_{\mathrm{e}}$ is expressed as

$$\boldsymbol{S}_{\mathrm{e}} = \int_{\Gamma_{\mathrm{e,PMa}}} \boldsymbol{N}_{\mathrm{a}}^{\mathrm{T}} (\boldsymbol{N}_{\mathrm{a}} - \boldsymbol{N}_{\mathrm{b}}) dA - \int_{\Gamma_{\mathrm{e,PMb}}} \boldsymbol{N}_{\mathrm{b}}^{\mathrm{T}} (\boldsymbol{N}_{\mathrm{a}} - \boldsymbol{N}_{\mathrm{b}}) dA. \tag{9}$$

Here, $\boldsymbol{N}_{\mathrm{a}}$ and $\boldsymbol{N}_{\mathrm{b}}$ are the shape function at nodes on $\Gamma_{\mathrm{e,PMa}}$ and $\Gamma_{\mathrm{e,PMb}}$. As presented in Figure 2, PM is discretized using eight-node hexahedral FEs. The function of $\boldsymbol{N}_{\mathrm{a}}$ and $\boldsymbol{N}_{\mathrm{b}}$ is presented later herein. Considering the other three boundary conditions, the semi-discretized equation of Eq. (7) is expressed in the following matrix form

$$\boldsymbol{M}\ddot{\boldsymbol{p}} + c_0^2\boldsymbol{K}^{'}\boldsymbol{p} + c_0\boldsymbol{C}^{'}\dot{\boldsymbol{p}} = \boldsymbol{f}, \tag{10}$$

with

$$\boldsymbol{K}^{'} = \boldsymbol{K} + \tfrac{\rho_0}{M}\boldsymbol{S}, \tag{11}$$

$$\boldsymbol{C}^{'} = \boldsymbol{C} + \tfrac{\rho_0 c_0}{R}\boldsymbol{S}. \tag{12}$$

Here, $\boldsymbol{M}$, $\boldsymbol{K}$, and $\boldsymbol{C}$ respectively represent the global mass matrix, global stiffness matrix, and global dissipation matrix in terms of the air domain. The global matrix related to PM element is represented by $\boldsymbol{S}$. The two vectors $\boldsymbol{p}$ and $\boldsymbol{f}$ represent the sound pressure at all nodes and the external force.

Furthermore, the spatially discretized matrix equation of Eq. (10) is discretized in a temporal direction with a direct time integration method called Newmark β method [21, 22] in which the sound pressure and its first derivative value are approximated as

$$\boldsymbol{p}^{n+1} = \boldsymbol{p}^n + \Delta t\dot{\boldsymbol{p}}^n + \Delta t^2(0.5-\beta)\ddot{\boldsymbol{p}}^n + \Delta t^2\beta\ddot{\boldsymbol{p}}^{n+1}, \tag{13}$$

$$\dot{\boldsymbol{p}}^{n+1} = \dot{\boldsymbol{p}}^n + 0.5\Delta t(\ddot{\boldsymbol{p}}^n + \ddot{\boldsymbol{p}}^{n+1}). \tag{14}$$

Therein, n, Δt, and β respectively represent the time step, time interval, and a parameter related to the accuracy and stability of Newmark β method [21, 22]. As described in this paper, we use Fox–Goodwin method, which is a highly accurate method using $\beta = 1/12$. Using Eqs. (13) and (14), the semi-discretized matrix equation (10) can be transformed into the following linear system of equations:

$$[\boldsymbol{M} + \beta\Delta t^2 c_0^2\boldsymbol{K}^{'} + 0.5c_0\Delta t\boldsymbol{C}^{'}]\ddot{\boldsymbol{p}}^{n+1} = \boldsymbol{f}^{n+1} - c_0\boldsymbol{C}^{'}\boldsymbol{P} - c_0^2\boldsymbol{K}^{'}\boldsymbol{Q}, \tag{15}$$

with

$$\boldsymbol{P} = \dot{\boldsymbol{p}}^n + 0.5\Delta t\ddot{\boldsymbol{p}}^n, \tag{16}$$

$$\boldsymbol{Q} = \boldsymbol{p}^n + \Delta t\dot{\boldsymbol{p}}^n + \Delta t^2(0.5-\beta)\ddot{\boldsymbol{p}}^n. \tag{17}$$

The linear system of equations is solved using a preconditioned iterative solver, Conjugate Gradient (CG) method [23], with diagonal scaling. As described above, the present time marching scheme is implicit. It consists of Eqs. (13)–(17). In the present scheme, sparse matrix storage formats [24] such as compressed row storage and compressed column storage formats are useful to store the global matrices $\boldsymbol{M}$, $\boldsymbol{K}^{'}$, and $\boldsymbol{C}^{'}$, which are sparse matrices with many zero components. Using sparse storage formats, the required memory of the present TD-FEM can be reduced considerably because it does not store zero components in the matrices. The main operation of present TD-FEM is the solution of a linear system of equations Eq. (15) and the two sparse matrix-vector products $\boldsymbol{C}^{'}\boldsymbol{P}$ and $\boldsymbol{K}^{'}\boldsymbol{Q}$ at the right-hand side of Eq. (15).

2.3. Eight-node hexahedral limp PM elements

As shown in the preceding section, limp PM elements are expressed as the third equation of Eq. (8). Only the components of matrix $\boldsymbol{S}_{\mathrm{e}}$ change according to element types for spatial discretization. This section presents detailed procedures used to derive hexahedral limp PM elements for three-dimensional analyses. For convenience, the matrix components of $\boldsymbol{S}_{\mathrm{e}}$ for rectangular elements are presented explicitly. Here, we assumed that the absorbing surfaces $\Gamma_{\mathrm{e,PMa}}$ and $\Gamma_{\mathrm{e,PMb}}$ respectively denote compositions of nodes 1–4–8–5 and nodes 2–3–7–6. Then, the node number within an element is given as shown in Figure 2. The element thickness is assumed to be zero: each nodal pair has the same coordinate. For example, nodes 1 and 2 are located on the same coordinate. This is true for the remaining nodal pairs as well: nodes 3–4, nodes 5–6, and nodes 7–8. Table 1 presents the shape function of eight-node hexahedral limp PM elements. The eight-node hexahedral limp PM elements are derived by performing two-dimensional Gauss-quadrature rules with two integration points at each direction after substituting the shape function into Eqs. (8) and (9). As one example of the resulting matrix expression, the matrix components for rectangular elements are given as

$$\boldsymbol{S}_{\mathrm{e}} = \frac{A_{\mathrm{e}}}{36}\begin{bmatrix} 4 & -4 & -2 & 2 & 2 & -2 & -1 & 1 \\ -4 & 4 & 2 & -2 & -2 & 2 & 1 & -1 \\ -2 & 2 & 4 & -4 & -1 & 1 & 2 & -2 \\ 2 & -2 & -4 & 4 & 1 & -1 & -2 & 2 \\ 2 & -2 & -1 & 1 & 4 & -4 & -2 & 2 \\ -2 & 2 & 1 & -1 & -4 & 4 & 2 & -2 \\ -1 & 1 & 2 & -2 & -2 & 2 & 4 & -4 \\ 1 & -1 & -2 & 2 & 2 & -2 & -4 & 4 \end{bmatrix}, \tag{18}$$

where A_e is the area of an absorbing surface.

2.4. Stability condition

At this stage, we are unable to derive a stability condition for case with PMs, but we have confirmed that the use of slightly smaller value than a critical time interval calculated using a stability condition for case without PMs was performed well for all numerical experiments conducted in the present study. Therefore, we present the stability conditions for a case without PMs to help how to set time interval for the case with PM. Derivation of the exact stability condition for the case with PMs is a subject of our future study.

The stability condition of present TD-FEM without PMs to obtain a critical time interval Δt_crit is given as [13]

$$\Delta t_\mathrm{crit} \leq \frac{1}{\omega_\mathrm{max}\sqrt{0.25-\beta}}. \tag{19}$$

Here, the maximum natural frequency ω_max is calculated by solving a generalized eigenvalue problem $(\boldsymbol{k}_\mathrm{e} - k^2\boldsymbol{m}_\mathrm{e})\boldsymbol{p}_\mathrm{e} = 0$ for all elements, where $\boldsymbol{k}_\mathrm{e}$, $\boldsymbol{m}_\mathrm{e}$ and k respectively represent the element stiffness, element mass matrices, and a numerical wave number as a solution. The computational cost of solving the eigenvalue problem is trivial because it is performed at the element matrix level. Furthermore, when one uses rectangular FEs, the critical time interval is calculable from a simple equation, which uses only sound speed in air c_0 and element size in each direction, as

$$\Delta t_\mathrm{crit} \leq \frac{1}{c_0\sqrt{\frac{1}{d_x^2}+\frac{1}{d_y^2}+\frac{1}{d_z^2}}}, \tag{20}$$

where d_x, d_y and d_z are the element size of an eight-node hexahedral rectangular element in x, y, and z directions. Because the stability condition of TD-FEM using eight-node hexahedral FEs with MIR is relaxed compared to the stability condition without MIR, then the present TD-FEM can use time interval $\sqrt{2}$ times greater than the value in the case without MIR. As reference, the stability condition for the case without MIR is given below:

$$\Delta t_\mathrm{crit} \leq \frac{1}{\sqrt{2}c_0\sqrt{\frac{1}{d_x^2}+\frac{1}{d_y^2}+\frac{1}{d_z^2}}}. \tag{21}$$

Table 1: Shape function of eight-node hexahedral PM elements, in which absorbing surfaces of PM, $\Gamma_{\mathrm{e,PMa}}$ and $\Gamma_{\mathrm{e,PMb}}$, consist respectively of nodes 1–4–8–5 and 2–3–7–6, as in Fig. 2.

	i=1, 2	i=4, 3	i=8, 7	i=5, 6
$N_{\mathrm{a\,or\,b},i}$	$\frac{1}{4}(1-\eta)(1-\zeta)$	$\frac{1}{4}(1+\eta)(1-\zeta)$	$\frac{1}{4}(1+\eta)(1+\zeta)$	$\frac{1}{4}(1-\eta)(1+\zeta)$
$\frac{\partial N_{\mathrm{a\,or\,b},i}}{\partial \eta}$	$-\frac{1}{4}(1-\zeta)$	$\frac{1}{4}(1-\zeta)$	$\frac{1}{4}(1+\zeta)$	$-\frac{1}{4}(1+\zeta)$
$\frac{\partial N_{\mathrm{a\,or\,b},i}}{\partial \zeta}$	$-\frac{1}{4}(1-\eta)$	$-\frac{1}{4}(1+\eta)$	$\frac{1}{4}(1+\eta)$	$\frac{1}{4}(1-\eta)$

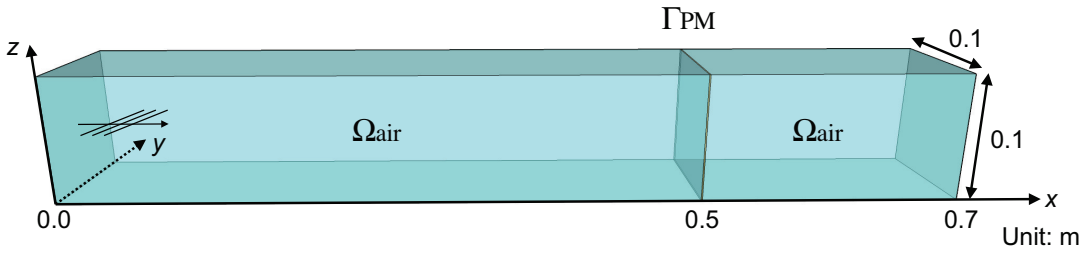

Figure 3: Plane wave propagation problem in an impedance tube with a single-leaf PM absorber. The backing air cavity depth is 0.2 m.

3. Impedance tube problems

A plane wave propagation problem in an impedance tube with a single-leaf PM absorber with a rigid backed air cavity (PMSG) is useful as a benchmark problem to verify the present limp PM model and to demonstrate the solution convergence of present TD-FEM. Figure 3 shows the impedance tube problem with PMSG. Using the present TD-FEM, the surface impedance and absorption coefficient of PMSG at normal incidence were calculated for cases with three permeable membranes, each having different flow resistance and surface density. The surface impedance was calculated directly from the ratio between sound pressure and particle velocity on the absorber surface, in which respective time responses were Fourier transformed into frequency domain. The accuracy and convergence of present TD-FEM were examined by comparison with an existing theoretical solution of the absorption characteristics of PMSG. Details of the theoretical solution are presented in Sec. 3.2. Three FE meshes with different spatial resolution were used to demonstrate convergence of the solution, in which time intervals were set respectively to slightly smaller values than their critical values calculated for a case without

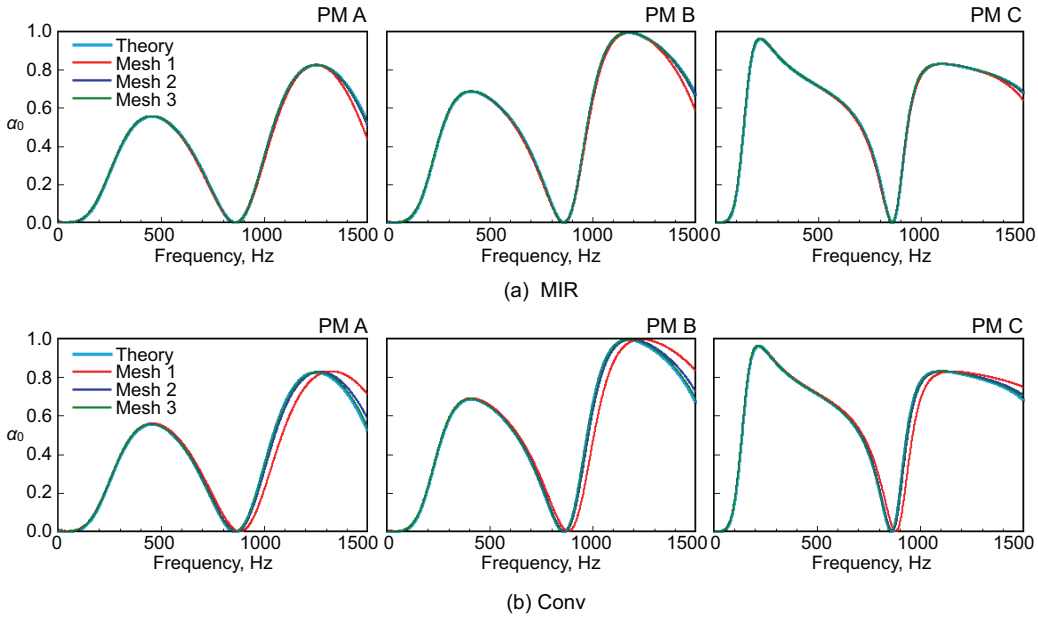

Figure 4: Theoretical normal incidence absorption coefficient of three PMSG with different permeable membranes versus those calculated using TD-FEM with (a) MIR and (b) Conv for three FE meshes: Mesh 1–Mesh 3.

permeable membranes. Furthermore, we conducted numerical experiments using conventional air FEs without MIR to demonstrate the effectiveness of using MIR.

3.1. Setup of FE analyses

Three PMs, each with different flow resistance R and surface density M were installed, respectively, with rigid-backed air cavities of 0.2 m depth: (1) PM A of $R = 196$ Pa$\cdot$s/m, $M = 0.065$ kg/m^2; (2) PM B of $R = 462$ Pa$\cdot$s/m, $M = 0.12$ kg/m^2 and (3) PM C of $R = 1087$ Pa$\cdot$s/m, $M = 0.495$ kg/m^2. A modulated Gaussian pulse was given as a volume acceleration waveform on the tube inlet with the upper-limit frequency of 1.5 kHz. Three FE meshes, Mesh 1–Mesh 3, discretized using cubic elements, have respective spatial resolutions of 4.6, 9.2, and 18.3 nodes per wavelength at the upper limit frequency. Corresponding element sizes for the three meshes are, respectively, 0.05 m, 0.025 m, and 0.0125 m. For the present TD-FEM the critical time intervals Δt_{crit} calculated using Eq. (20) are 8.3990×10^{-5} s (Mesh 1), 4.1995×10^{-5} s (Mesh 2), and 2.0998×10^{-5} s (Mesh 3). Additionally, Δt_{crit}s for

the use of conventional air FEs by Eq. (21) are 5.9390 $\times$ 10^{-5} s (Mesh 1), 2.9695 $\times$ 10^{-5} s (Mesh 2), and 1.4848 $\times$ 10^{-5} s (Mesh 3). According to the critical time interval values for the present TD-FEM time interval, Δts were set to 8.3333 $\times$ 10^{-5} s (Mesh 1), 4.1668 $\times$ 10^{-5} s (Mesh 2), and 2.0833 $\times$ 10^{-5} s (Mesh 3). For the use of conventional air FEs, Δt were set to 5.5556 $\times$ 10^{-5} s (Mesh 1), 2.7778 $\times$ 10^{-5} s (Mesh 2), and 1.3889 $\times$ 10^{-5} s (Mesh 3). Regarding the boundary conditions of tube, the tube inlet is a perfectly absorbing boundary with characteristic impedance of air. The remaining boundaries are rigid. Convergence tolerance of 10^{-6} was used in a stopping criterion of the iterative solver.

3.2. Theoretical absorption characteristics of PMSG

According to the literature [1], the normalized surface impedance z_{n} of an infinitely large PMSG can be expressed as

$$z_{\mathrm{n}} = \left(\frac{\rho_0 c_0}{R} + \frac{\rho_0 c_0}{i\omega M} \right)^{-1} - \frac{i}{\cos\theta} \cot(kD\cos\theta), \tag{22}$$

where D and θ respectively represent the air cavity depth and sound incident angle. In Eq. (22), the first and second terms are, respectively, the transfer impedance of limp PM and the acoustic impedance of a rigid backed air cavity. This model includes the assumption that a PM itself is a locally reacting material as expressed in its transfer impedance. However, the acoustic impedance of air cavity is dependent on the incident angle of sound wave, with the result that PMSG acts as a non-locally reacting sound absorbing structure. The oblique incidence absorption coefficient α_θ and the statistical absorption coefficient α_{s} were calculated from the following equations.

$$\alpha_\theta = \frac{4\mathrm{Re}[z_{\mathrm{n}}]\cos\theta}{(\mathrm{Re}[z_{\mathrm{n}}]\cos\theta + 1)^2 + (\mathrm{Im}[z_{\mathrm{n}}]\cos\theta)^2}. \tag{23}$$

$$\alpha_{\mathrm{s}} = \frac{\int_0^{\pi/2} \alpha_\theta \sin\theta\cos\theta d\theta}{\int_0^{\pi/2} \sin\theta\cos\theta d\theta}. \tag{24}$$

3.3. Results and discussion

Figures 4(a) and 4(b) respectively show normal incidence absorption coefficients of PMSG with PM A–PM C calculated using the theory, presenting TD-FEM with MIR (MIR) and without MIR (Conv) for Mesh 1 – Mesh 3.

For both MIR and Conv, discrepancies from the theory are visible for the results of Mesh 1. For respective methods, using higher spatial resolution meshes produces better agreement with the theoretical value. This is true also for the entire results of PM A–PM C. However, the agreement with theory is better for MIR. Discrepancies in the results of MIR can be found at around 1.5 kHz, where the absorption coefficients are slightly lower than the theoretical values. The discrepancies of Conv appear at lower frequencies, and a notch frequency and a second peak frequency shift to higher frequencies than their theoretical values. Table 2 presents calculated second peak frequency by MIR and Conv for PM A – PM C, where a relative error from a theoretical second peak frequency is also presented. The theoretical second peak frequencies for cases with PM A – PM C are, respectively, 1,252 Hz, 1,174 Hz, and 1,100 Hz. The relative error of Conv is greater than 5% for Mesh 1; the value still exceeds 1% for Mesh 2. However, the relative error of MIR is lower than 0.82% even in Mesh 1, which shows better agreement than the result in Mesh 2 of Conv. Figures 5(a) and 5(b) present comparison of normalized surface impedance of PMSG using PM C between theory and (a) MIR and (b) Conv, for Mesh 1. For both MIR and Conv the real part agrees well with the theoretical value. Discrepancies appear in only for the imaginary part. The discrepancies in the imaginary part are attributable to reduction of the approximation accuracy in reactance of the rigid-backed air cavity. In time domain finite element analyses, the use of an insufficient resolution mesh produces dispersion error at higher frequencies, which means that the sound speed changes from the exact value at higher frequencies. In addition, as presented in Eq. (22), the surface impedance of a rigid-backed air cavity is a purely imaginary value. Therefore, discrepancies in the surface impedance appear only in the reactance. The imaginary part of surface impedance determines the notch and peak frequencies of the absorption coefficient. This is the reason underlying the change of the notch and peak frequencies in Mesh 1 of Conv. It is noteworthy that although the transfer impedance of limp PM includes a mass reactance term, the term only affects surface impedance at low frequencies.

The accuracy of MIR and Conv is evaluated further using RMS error α_{rms} between theoretical absorption coefficient $\alpha_{\mathrm{theory}}(f)$ and numerical absorption coefficient $\alpha_{\mathrm{FEM}}(f)$, where f is the frequency. The RMS error is

Table 2: Second peak frequency of MIR and Conv. for Mesh 1– Mesh 3, and relative error from theoretical frequency. The theoretical second peak frequencies are 1,252 Hz, 1,174 Hz, and 1,100 Hz, respectively, for PM A, PM B, and PM C.

	Mesh	MIR	Conv
PM A	1	1,252 Hz (0.00%)	1,327 Hz (5.99%)
	2	1,253 Hz (0.08%)	1,271 Hz (1.52%)
	3	1,253 Hz (0.08%)	1,257 Hz (0.40%)
PM B	1	1,180 Hz (0.51%)	1,239 Hz (5.54%)
	2	1,176 Hz (0.17%)	1,190 Hz (1.36%)
	3	1,174 Hz (0.00%)	1,178 Hz (0.34%)
PM C	1	1,109 Hz (0.82%)	1,157 Hz (5.18%)
	2	1,102 Hz (0.18%)	1,114 Hz (1.27%)
	3	1,101 Hz (0.09%)	1,103 Hz (0.27%)

calculated at 1/3 octave band center frequencies and defined as

$$\alpha_{\mathrm{rms}} = \sqrt{\frac{1}{N_{\mathrm{f}}} \sum_{f=f_{\mathrm{l}}}^{f_{\mathrm{u}}} [\alpha_{\mathrm{FEM}}(f) - \alpha_{\mathrm{Theory}}(f)]^2}, \tag{25}$$

where N_{f}, f_{l}, and f_{u} respectively represent the number of frequencies including 1/3 oct. band, lower and upper limit frequencies of 1/3 oct. band. Figures 6(a)–6(c) respectively present comparisons of the RMS errors in MIR and Conv for PM A – PM C, as calculated for Mesh 1 – Mesh 3. Results demonstrate that the RMS errors in Mesh 1 of MIR are comparable or lower than those in Mesh 2 of Conv at higher frequencies. For Mesh 2 of MIR, as well, the RMS error is comparable to or lower than the result found for Mesh 3 of Conv. This value engenders reduction in the degrees of freedom by about one-eighth, and reduction in the time steps by $1/(2\sqrt{2})$: The computational cost of present TD-FEM with MIR is reduced to 1/23 of that using conventional air elements.

The results described above show that the present limp PM model was first verified. Results revealed that the present TD-FEM with MIR produces more accurate results than those obtained with conventional air FEs, with a lower spatial resolution mesh and fewer time steps.

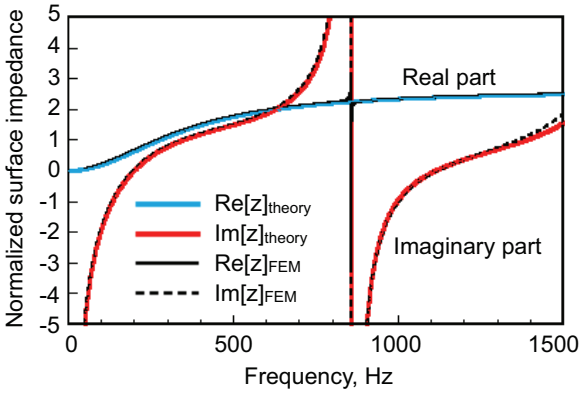

(a) MIR

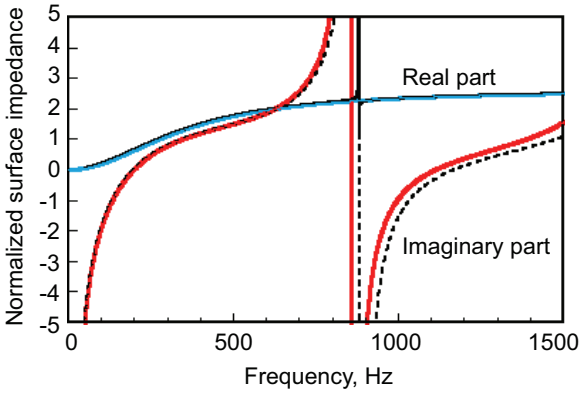

(b) Conv

Figure 5: Theoretical normalized surface impedance of PMSG with PM C versus those calculated using TD-FEM with (a) MIR and (b) Conv for Mesh 1.

4. Prediction of the reverberation absorption coefficient of PMSG

The prediction of absorption characteristics of PMSG in a diffuse sound field is useful to demonstrate the applicability of the present TD-FEM with the limp PM model. Here, large-scale analyses conducted using the present method, which simulate a reverberation absorption coefficient measurement, were undertaken to obtain reverberation absorption coefficients of eight PMSG, each having different material properties of PM. The calculated absorption coefficients were compared with measured values and theoretical statistical absorption coefficients. Table 3 presents the eight PMs used for measure-

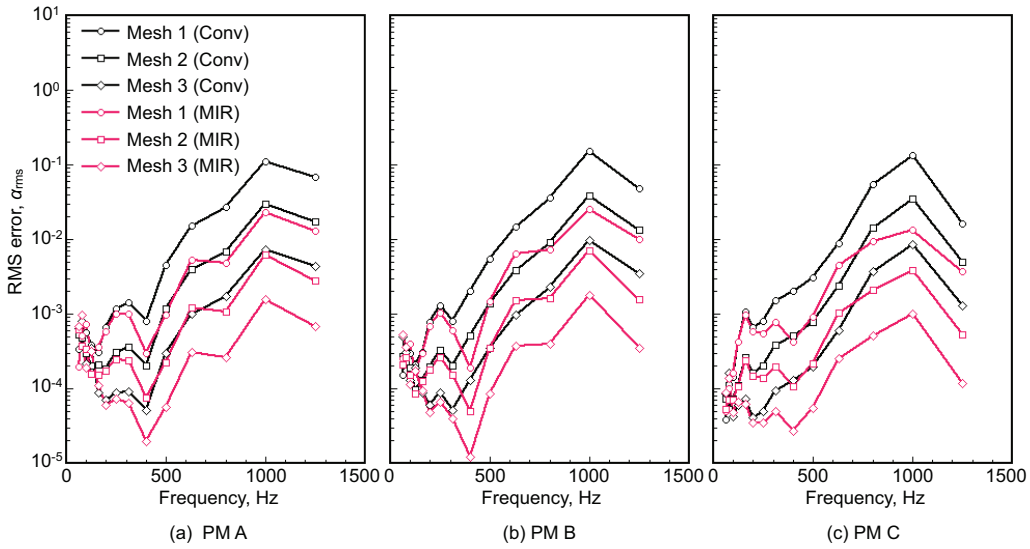

Figure 6: Comparison of RMS errors in absorption coefficients of MIR and Conv calculated using Mesh 1 – Mesh 3: (a) PM A, (b) PM B, and (c) PM C.

ments. The material properties are shown. All are measured values: flow resistance, surface density and thickness. They are all thin woven fabrics or non-woven fabrics made of general purpose chemical fibers such as polyethylene terephthalate (PET), polypropylene (PP), and glass fibers. The investigation ranges of material parameters are from $0.15\rho_0 c_0$ to $2.9\rho_0 c_0$ flow resistance, and from 0.06 kg/m^2 to 0.24 kg/m^2 surface density. The air cavity depth of PMSG is 0.1 m. The reverberation absorption coefficients of eight PMSG were measured in an irregularly shaped reverberation room (130 m^3 volume and 153 m^2 surface area) with non-parallel walls, based on JIS A 1409 standard (ISO 354 compatible), except for the area of the specimen. The area of the specimen is 6.0 m^2 (2.2 m $\times$ 2.73 m). The perimeter edges of the test specimen were covered with an acrylic frame. Then an integrated impulse response method was used to measure reverberation times in an empty room and in a room containing the test specimens. Two source positions and three microphone positions were used for each source. Figures 7(a) and 7(b) show measured reverberation times in the empty room and the average sound absorption coefficients. Figure 7(b) also shows the given absorption coefficient in FEM analyses. As shown in the figure, the average sound absorption coefficient increases slightly with increasing frequency. To

Table 3: Material parameters of eight permeable membranes #1–#8: flow resistance R, surface density M, and thickness t, which are measured values. Flow resistance was measured using the direct flow method.

Permeable membrane	R, Pa s/m	M, kg/m^2	t, mm
#1 PET cloth A	196 ($0.47\rho_0 c_0$)	0.06	0.16
#2 PET cloth B	462 ($1.12\rho_0 c_0$)	0.12	0.20
#3 Glass fiber cloth	1200 ($2.90\rho_0 c_0$)	0.21	0.18
#4 PET high-density woven fabric	1050 ($2.54\rho_0 c_0$)	0.20	0.48
#5 PP non-woven fabric A	64 ($0.15\rho_0 c_0$)	0.13	0.39
#6 PP non-woven fabric B	221 ($0.53\rho_0 c_0$)	0.24	0.59
#7 PET non-woven fabric A	70 ($0.17\rho_0 c_0$)	0.08	0.31
#8 PET non-woven fabric B	80 ($0.19\rho_0 c_0$)	0.08	0.31

simulate the frequency dependence of absorption characteristics of the room's boundary surface, three frequency bands were considered in FEM analyses, as explained later. The Schroeder frequency of the empty room is 499 Hz. As explained in a later section, the measured and simulated reverberation absorption coefficients almost follow the theoretical statistical absorption coefficients. Therefore, we inferred that the measured and simulated results below the Schroeder frequency are reliable.

4.1. Outline of FE analysis

Two reverberation room models Model 1 and Model 2, each having a different absorber setup, were used for numerical analyses using the present TD-FEM. Figures 8(a) and 8(b) present the two models. In Model 1, which corresponds to the measurement condition, PMSG is located on the floor with a rigid partition covering of specimen. For model 2, a simpler model in the absorber setup, the backing air cavity of PMSG is located under the floor. Model 2 was used to reduce the computational cost of present TD-FEM by avoiding modeling complexity. Impulse responses in the room were calculated using the two models containing the absorber as well as an empty room model. Reverberation absorption coefficients were calculated further from reverberation times (T_{20}) in the empty room and in the room containing the absorber. Two point sources were placed in a corner of the room, as portrayed in Fig. 8. For each source, five microphone positions were considered. An impulse response of optimized FIR filter based on the Parks–McClellan algorithm was used as the sound source signal. Calculations were made for

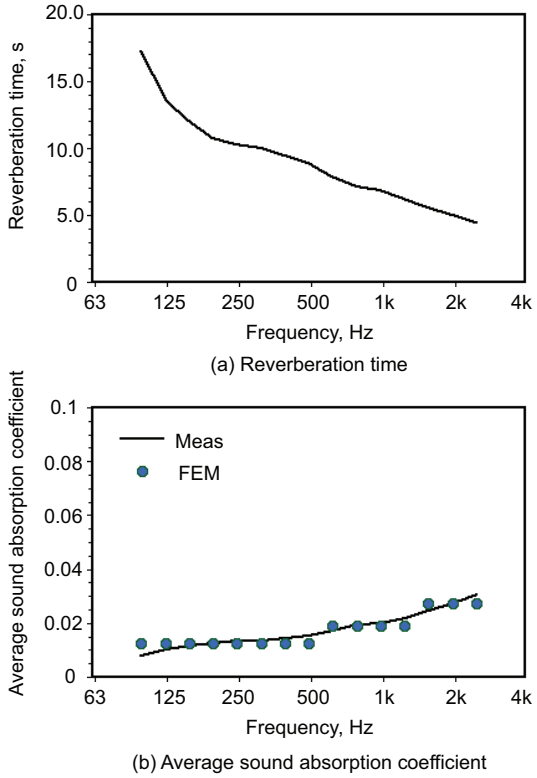

Figure 7: (a) Measured reverberation time in the empty room and (b) Average sound absorption coefficient in the empty room and given absorption coefficient in FEM analyses.

three frequency bands: low, medium, and high frequencies. Here, the low-frequency band includes frequencies of 100 Hz – 500 Hz. Mid-frequency and high-frequency bands respectively include frequencies of 630 Hz to 1.25 kHz, and from 1.6 kHz to 2.5 kHz. Figures 9(a) and 9(b) respectively show the sound source waveform and its frequency characteristics for the high-frequency band. The signal has flat amplitude at frequencies of 88–2,828 Hz. For low-frequency and mid-frequency bands, the frequency range of flat amplitude is from 88 Hz to 1414 Hz. The impulse responses in the room at low, medium and high frequency bands were, respectively, calculated up to 13.0 s, 9.0 s, and 5.0 s for the sound source signal. Then 1/3 oct. band filtering was performed at 1/3 oct. band center frequencies of 100 Hz to 2.5 kHz. Equivalent real impedance values corresponding to statistical absorption coefficients of 0.0124, 0.0189, and 0.0275 were given respectively to all

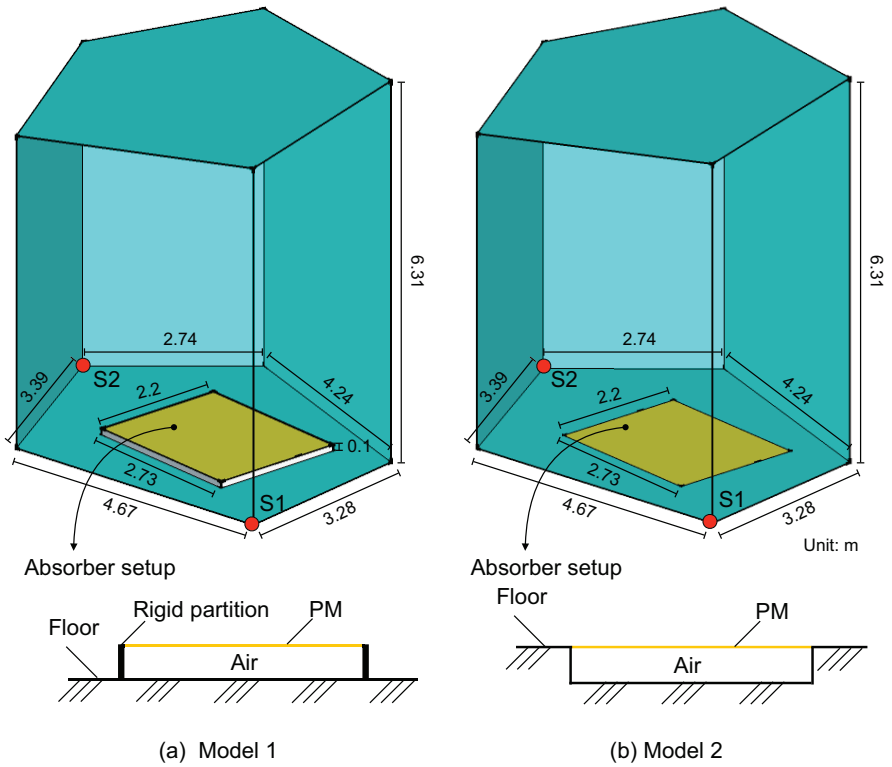

Figure 8: Two reverberation room models with different absorber setup for numerical simulation: (a) Model 1 and (b) Model 2. Model 1 is corresponding to actual measurement conditions. Model 2 is a simpler model in absorber setup.

the boundary surface of rooms for low, medium, and high frequency bands, as portrayed in Fig. 7(b). The statistical absorption coefficients correspond to the arithmetic mean value of average sound absorption coefficient in the empty room within the respective frequency bands. The convergence tolerance of the iterative solver is set as 10^{-6} for low-frequency and mid-frequency bands. The value is 10^{-4} for the high-frequency band.

For spatial discretization of the room models, two FE meshes with different spatial resolution were created for low and medium frequency bands and the high frequency band, which respectively satisfy five elements per wavelength at the upper-limit frequencies of 1,414 Hz and 2,828 Hz. As a reference, the resulting total numbers of elements of finer FE mesh for the high frequency band are 17,632,256 in the empty model, 18,608,148 in Model 1, and 17,734,408 in Model 2. For the high frequency band analyses the time

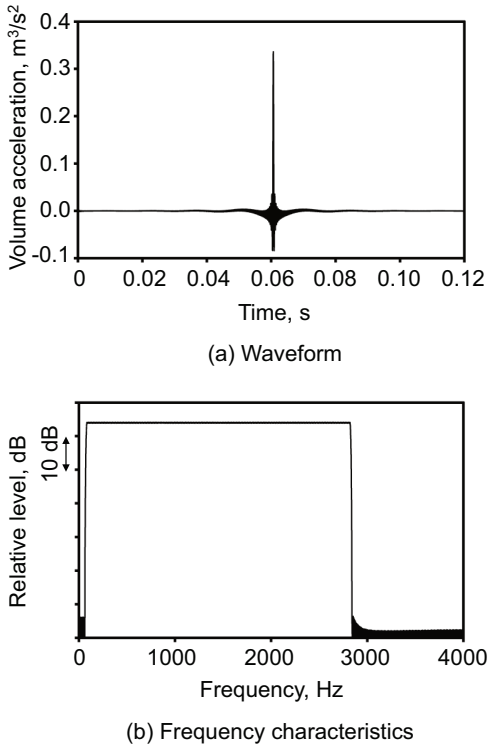

Figure 9: Sound source signal for numerical analysis: (a) waveform and (b) its frequency characteristics.

intervals Δt were set respectively to 1.2195×10^{-5} s for the empty and Model 2 and 1.14943×10^{-5} s for Model 1 considering their respective critical time intervals, which are 1.2578×10^{-5} s and 1.16797×10^{-5} s: $\Delta t = 0.9696\Delta t_{\mathrm{crit}}$ and $\Delta t = 0.9841\Delta t_{\mathrm{crit}}$ used respectively for the empty model, Model 2, and Model 1. As described in Sec. 2.4, use of the slightly smaller critical value performed well for a stable computation. Thereby, we can expect that the strategy would perform well in the range of material parameters of PM presented in Table 3. Furthermore, the same strategy was used for low and medium frequency band analyses. The comparison was taken up to 2.5 kHz because of the limitations of our computational environment.

4.2. Results and discussion

Figure 10 presents a comparison of reverberation absorption coefficients α_{r} of PMSG using membranes #1–#8 among measurement (Meas), numerical values using Model 1 and Model 2, and the theory. The absolute dif-

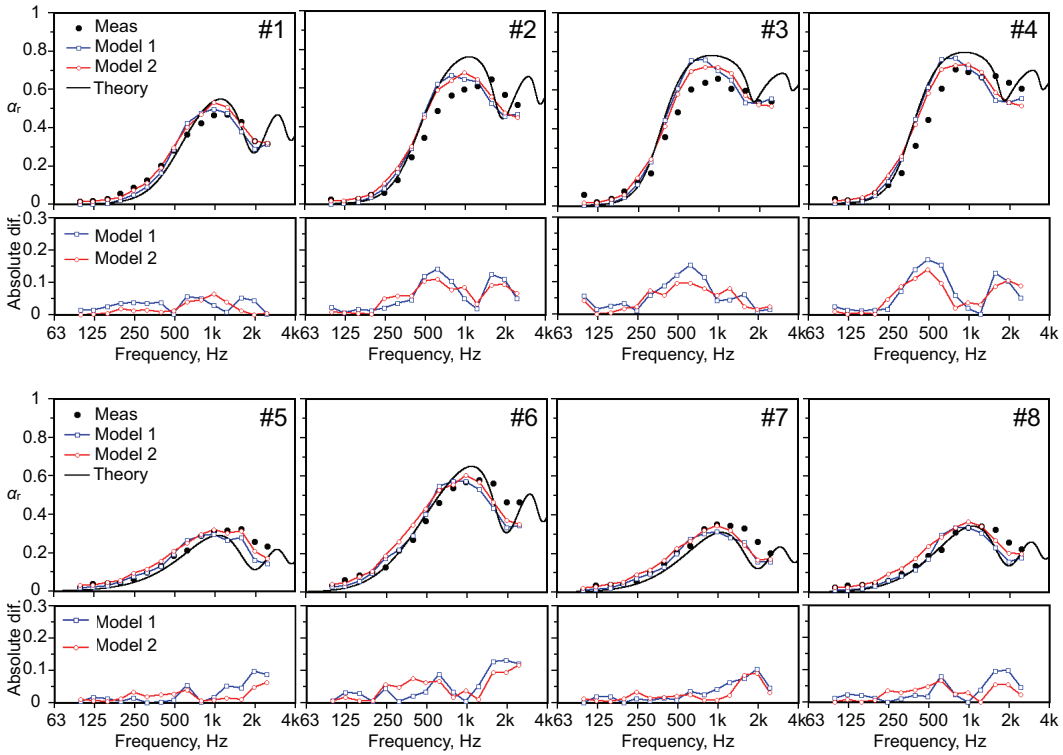

Figure 10: Comparison of reverberation absorption coefficient α_{r} of PMSG using membranes of #1–#8 among measurement, theory and numerical analyses using Model 1 and Model 2. Lower figures show the absolute difference between measured value and FEM values. Note that theoretical values are plotted as statistical absorption coefficients.

ference of the absorption coefficient between measurements and FEM is also shown in the figure. As a well known feature and as might be apparent in the theoretical statistical absorption coefficient, PMSG can not offer a high diffuse field absorption coefficient at low frequencies because of the effects of a non-locally reacting rigid-backed air cavity [1]. This feature can be found in both numerical and measured results. In addition, the measured and FEM results almost follow the theoretical values in the frequencies below the Schroeder frequency. Overall, considering measurement uncertainty, numerical results obtained using the two models agree well with measurement results.Specifically, better agreement was found for results for membranes #1, #5, #7, and #8, where mean absolute differences are less than 0.033 in both models. In all cases, the frequency characteristics of numerically

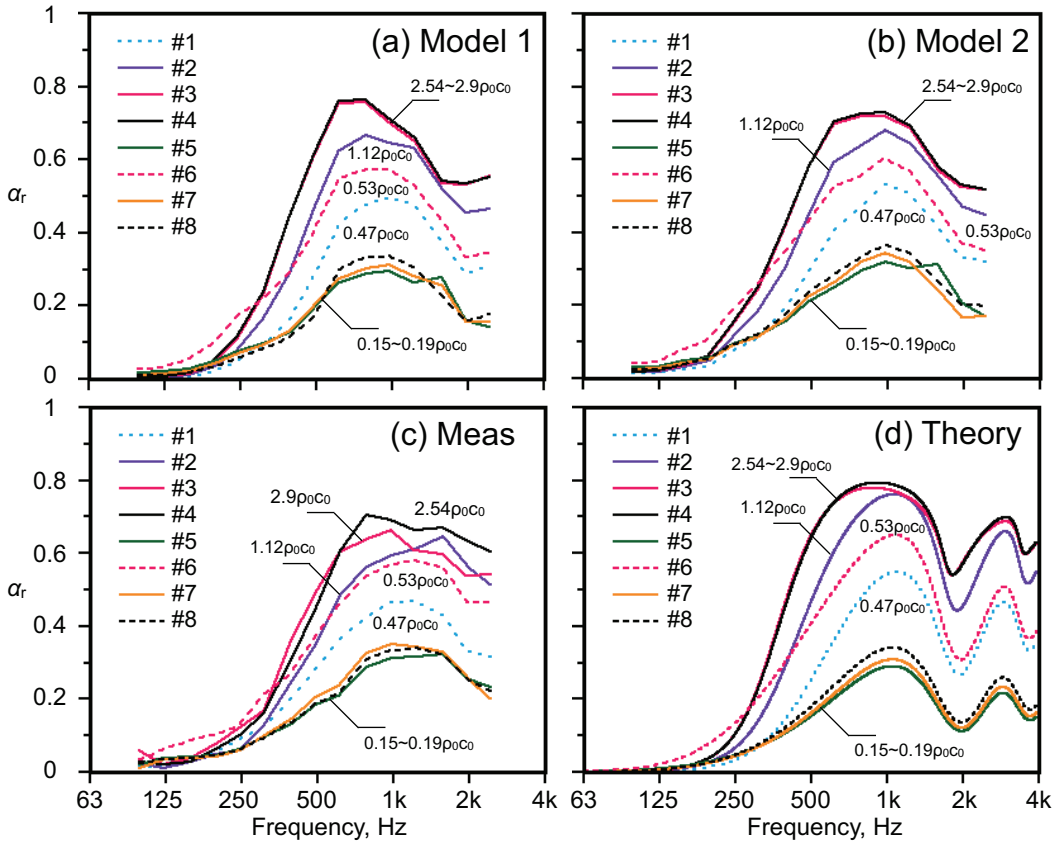

Figure 11: Magnitude relation of reverberation absorption coefficient α_r of PMSG using membranes of #1–#8: (a) numerical results obtained using Model 1 and (b) Model 2, (c) measurement results and (d) Theory. Note that theoretical values are plotted as statistical absorption coefficients.

calculated α_r are similar to those of measured and theoretical results. Great discrepancy from measured values can be found at around 500 Hz in the cases of PMs with high flow resistance, i.e., #2, #3, and #4. The FEM values in PMs #2, #3, and #4 are more consistent with the theoretical values obtained for frequencies around 500 Hz. The better agreement with theory is apparently natural because both the FEM and theory use the same transfer impedance model of PM without measurement errors in material properties of PM. However, at 1 kHz and 1.25 kHz, the FEM values show large discrepancy from the theory. This difference might be attributable to deterioration of the diffuseness of the sound field. At this stage, detailed investigations

of the reason for differences from measured and theoretical values are the subject of future research.

Regarding differences of results between Model 1 and Model 2, the two models show similar results, which have similar frequency error characteristics in the absolute difference. Apparently, the simpler model Model 2 performs well in the presented cases, as does the more compatible model with the measurements, i.e., Model 1. Perhaps for this reason, the area effect does not appear strongly because PMSG has a low grazing incidence absorption coefficient. In other words, a diffracted wave from perimeter edges of the specimen can not be absorbed effectively because of the low grazing incidence absorption coefficient.

Furthermore, we present the applicability of the present method from another perspective. Figures 11(a)–11(d) respectively present the magnitude relation of the reverberation absorption coefficient of PMSG using the eight membranes for numerical results (Model 1 and Model 2) and measurement results and theoretical results. The magnitude relation of numerical results is consistent with measured results and is more consistent with theoretical results. Again, the better agreement with theory is natural because the same transfer impedance model of PMs is used. In the measured and theoretical results, #3 and #4 membrane results show higher absorption by their high flow resistance. These results are also true for numerical results. Furthermore, membranes #1 and #6 have comparable flow resistance, but membrane #6 has four times greater mass. By virtue of the heavier mass, results obtained using membrane #6 show higher absorption than membrane #1. This relation is observed for numerical, measured, and theoretical results. Based on those results, we infer that the present TD-FEM can accurately capture the change of absorption characteristics of PMSG attributable to the material parameter differences of membranes.

5. Conclusions

This report presented three-dimensional TD-FEM for sound field analyses including PMs, with a limp PM model. The TD-FEM is based on the formulation described in our earlier report [13], which uses a dispersion reduced hexahedral linear FEs with MIR, and an iterative solver to solve the system of linear equations efficiently. The limp PM model was incorporated into the TD-FEM as a boundary condition. Also, hexahedral limp PM FEs were derived for three-dimensional analysis. Results from a plane-wave prop-

agation problem in an impedance tube with PMSG showed the validity of TD-FEM using the limp PM model. Results also show that the use of MIR performs well even for the case with limp PM FEs. Also, higher convergence to theoretical absorption coefficient is obtained compared to the case using conventional air FEs without MIR. Applicability of the present TD-FEM was examined further by comparison with measurements of reverberation absorption coefficients of PMSG, and with the corresponding theoretical statistical absorption coefficient. For comparison, we used PMs less than 1 mm thickness made of PET, PP, and glass fibers, each with the flow resistance of $0.15\rho_0 c_0$ to $2.9\rho_0 c_0$ and surface density of $M = 0.06$ kg/m^2 to 0.24 kg/m^2. Results revealed that the present TD-FEM is predictable the magnitude relation of absorption characteristics in PMSG attributable to the change of material properties of PM. However, in a quantitative sense, larger differences from measured and theoretical values were found in cases of PMs with high flow resistance. Further investigations clarifying the difference will be undertaken in future works.

Acknowledgments

This work was supported in part by JSPS KAKENHI Grant No. 17K14771. The computation was partly conducted using computer facilities at the Research Institute for Information Technology, Kyushu University.

References

[1] Ingard KU. "Sheet absorbers", in *Notes on Sound Absorption Technology*, Noise Control Foundation, New York, 1994, Chap. 1, pp1-1–1-16.

[2] Takahashi D, Sakagami K, Morimoto M. Acoustic properties of permeable membranes. J Acoust Soc Am 1996;99(5):3003–09.

[3] Sakagami K, Kiama M, Morimoto M, Takahashi D. Detailed analysis of the acoustic properties of a permeable membrane. Appl Acoust 1998;54(2):93–111.

[4] Pieren R. Sound absorption modeling of thin woven fabrics backed by an air cavity. Text Res J 2012;82(9):864–74.

[5] Sakagami K, Yoshida K, Morimoto M. A note on the acoustics properties of a double-leaf permeable membrane. Acoust Sci and Tech 2009;30(5):390–2.

[6] Sakagami K, Funahashi K, Somatomo Y, Okuzono T, Nishikawa C, Toyoda M. An experimental study on the absorption characteristics of a three-dimensional permeable membrane space sound absorber. Noise Control Engr J 2015;63(3):300–7.

[7] Pieren R, Heutschi K. Predicting sound absorption coefficients of lightweight multilayer curtains using the equivalent circuit method. Appl Acoust 2015;92:27–41.

[8] Botteldooren D. Finite-difference time-domain simulation of low-frequency room acoustics problems. J Acoust Soc Am 1995;98(6):3302–08.

[9] Sakamoto S. Phase-error analysis of high-order finite-difference time-domain scheme and its influence on calculation results of impulse response in closed sound field. Acoust Sci and Tech 2007;28(5):295–309.

[10] Sakamoto S, Nagatomo H, Ushiyama A, Tachibana H. Calculation of impulse responses and acoustic parameters in a hall by the finite-difference time-domain method. Acoust Sci and Tech 2008;29(4):256–65.

[11] Otsuru T, Tomiku R. Basic characteristics and accuracy of acoustic element using spline function in finite element sound field analysis. Acoust Sci and Tech 2001;21(2):87–95.

[12] Okuzono T, Otsuru T, Tomiku R, Okamoto N. Fundamental accuracy of time domain finite element method for sound field analysis of rooms. Appl Acoust 2010;71(10):940–46.

[13] Okuzono T, Otsuru T, Tomiku R, Okamoto N. Application of modified integration rule to time-domain finite element acoustic simulation of rooms. J Acoust Soc Am 2012;132(2):804–13.

[14] Okuzono T, Otsuru T, Tomiku R, Okamoto N. A finite-element method using dispersion reduced spline elements for room acoustics simulation. Appl Acoust 2014;79:1–8.

[15] Mehra R, Raghuvanshi N, Savioja L, Lin MC, Manocha D. An efficient GPU-based time domain solver for the acoustic wave equation. Appl Acoust 2012;73:83–94.

[16] Simonaho SP, Lähivaara T, Huttunen T. Modeling of acoustic wave propagation in time-domain using the discontinuous Galerkin method– A comparison with measurements. Appl Acoust 2012;73:173–83.

[17] Hornikx M, Krijnen T, van Harten L. openPTSD:The open source pseudo-spectral time-domain method for acoustic propagation. Comput Phys Communications 2016;203:298–308.

[18] Okuzono T, Sakagami K. A time-domain finite element model of permeable membrane absorbers. Acoust Sci and Tech 2016;37(1):46–49.

[19] Sakuma T, Iwase T, Yasuoka M, Prediction of sound fields in rooms with membrane materials – Development of a limp membrane element in acoustical FEM analysis and its application –. J Archit Plann Environ Eng 1998;505:1–8.

[20] Yue B, Guddati MN, Dispersion-reducing finite elements for transient acoustics. J Acoust Soc Am 2005;118(4):2132–41.

[21] Newmark NM, A method of computation for structural dynamics. J Eng Mech Div 1959;85:67–94.

[22] Hughes TJR, The finite element method linear static and dynamic finite element analysis. Dover; 2000.

[23] Barrett R, Berry M, Chan TF, Demmel J, Donato J, Dongarra J, Eijkhout V, Pozo R, Romine C, van der Vorst H. "Nonstationary iterative methods", in *Templates for the solution of linear systems: Building blocks for iterative methods*, SIAM, Philadelphia, 1994, Chap. 2.3, pp. 14–30.

[24] Barrett R, Berry M, Chan TF, Demmel J, Donato J, Dongarra J, Eijkhout V, Pozo R, Romine C, van der Vorst H. "Data structures", in *Templates for the solution of linear systems: Building blocks for iterative methods*, SIAM, Philadelphia, 1994, Chap. 4.3, pp. 64–76.